scientific reports

Check for updates

OPEN

Autism-associated mutation in Hevin/Sparcl1 induces endoplasmic reticulum stress through structural instability

Takumi Taketomi[1], Takunori Yasuda[2], Rikuri Morita[3], Jaehyun Kim[2], Yasuteru Shigeta[1,3], Cagla Eroglu[6,7], Ryuhei Harada[2,3] & Fuminori Tsuruta[1,2,4,5]✉

Hevin is a secreted extracellular matrix protein that is encoded by the *SPARCL1* gene. Recent studies have shown that Hevin plays an important role in regulating synaptogenesis and synaptic plasticity. Mutations in the *SPARCL1* gene increase the risk of autism spectrum disorder (ASD). However, the molecular basis of how mutations in *SPARCL1* increase the risk of ASD is not been fully understood. In this study, we show that one of the *SPARCL1* mutations associated with ASD impairs normal Hevin secretion. We identified Hevin mutants lacking the EF-hand motif through analyzing ASD-related mice with vulnerable spliceosome functions. Hevin deletion mutants accumulate in the endoplasmic reticulum (ER), leading to the activation of unfolded protein responses. We also found that a single amino acid substitution of Trp^{647} with Arg in the EF-hand motif associated with a familial case of ASD causes a similar phenotype in the EF-hand deletion mutant. Importantly, molecular dynamics (MD) simulation revealed that this single amino acid substitution triggers exposure of a hydrophobic amino acid to the surface, increasing the binding of Hevin with molecular chaperons, BIP. Taken together, these data suggest that the integrity of the EF-hand motif in Hevin is crucial for proper folding and that ASD-related mutations impair the export of Hevin from the ER. Our data provide a novel mechanism linking a point mutation in the *SPARCL1* gene to the molecular and cellular characteristics involved in ASD.

Autism spectrum disorder (ASD) is a prevalent neurodevelopmental disorder characterized by impaired social interaction and behaviors. Congenital genetic defect is one of the causes of ASD. To date, many genes associated with ASD have been identified by several genome-wide association studies[1–5]. Mostly, these mutations are found in the genes encoding synaptic proteins, transcription factors, chromatin modifiers, and protein metabolisms. Hence, dysfunctions of these proteins caused by both de novo and inherited mutations are highly linked to the pathogenesis of ASD.

An aberrant ubiquitin–proteasome system is one of the main causes of ASD pathogenesis. The deubiquitinating enzyme, USP15, which regulates various signaling pathways and cellular processes, is involved in neuronal disorders[6–8]. Moreover, de novo mutation in the *Usp15* gene is closely associated with ASD[2,9,10]. Previously, we have reported that USP15 deubiquitinates U6 snRNA-specific terminal uridylyl transferase 1 (TUT1) and regulates the spliceosome cascade[11]. A defect in *Usp15* increases the probability of splicing errors and produces various abnormal variants. We also found that impaired USP15 induces the endoplasmic reticulum (ER) stress, although the mechanism linking splicing error to ER stress has not yet been clarified[11].

[1]Ph.D. Program in Human Biology, School of Integrative and Global Majors, University of Tsukuba, 1-1-1 Tennodai, Tsukuba, Ibaraki, 305-8577, Japan. [2]Master's and Doctoral Program in Biology, School of Life and Environmental Sciences, University of Tsukuba, 1-1-1 Tennodai, Tsukuba, Ibaraki 305-8577, Japan. [3]Center for Computational Sciences, University of Tsukuba, 1-1-1 Tennodai, Tsukuba, Ibaraki 305-8577, Japan. [4]Master's and Doctoral Program in Neuroscience, Graduate School of Comprehensive Human Sciences, University of Tsukuba, 1-1-1 Tennodai, Tsukuba, Ibaraki 305-8577, Japan. [5]Ph.D. Program in Humanics, School of Integrative and Global Majors, University of Tsukuba, 1-1-1 Tennodai, Tsukuba, Ibaraki 305-8577, Japan. [6]Department of Cell Biology, Duke University Medical Center, Durham, NC 27710, USA. [7]Howard Hughes Medical Institute, Duke University Medical Center, Durham, NC 27710, USA. ✉email: tsuruta.fuminori.fn@u.tsukuba.ac.jp

Proper subcellular localization of the synaptic proteins is crucial for regulating neural circuit formation and brain homeostasis. The amino acid substitutions in synaptic proteins result in their accumulation in the ER, and cause abnormal trafficking to the proper sites. It is also known that these substitutions impair protein folding and frequently activate the unfolded protein response (UPR). For instance, the ASD-associated mutant Neuroligin 4 (NL4) , in which Arg^{87} is replaced with Trp, accumulates in the ER and does not transport to neuronal dendrites[12]. The ASD-associated γ-aminobutyric acid transporter 1 (GAT-1) mutant, in which Pro^{361} is replaced with Thr, is prone to localize in the ER[13]. Moreover, missense mutations of novel ASD-associated transmembrane proteins, a cell adhesion molecule-1 (CADM1), and contactin-associated protein-like 2 (CASPR2) are also localized in the ER and upregulates ER stress[14,15]. Therefore, abnormal amino acid substitutions of the ASD-related synaptic proteins are predisposed to accumulate in the ER and hamper their trafficking to the proper sites, attenuating innate synaptic functions.

Hevin, also known as secreted protein acidic and rich in cysteine-like 1 (Sparcl1), is a secreted protein. The C-terminus of Hevin has an amino acid sequence with approximately 60% identity to Sparc. It has been reported that Hevin and its family proteins are involved in metastasis, inflammation, angiogenesis, and apoptosis[16]. In the central nervous system, Hevin is predominantly expressed in astrocytes and is expressed in neurons to a lesser extent[17]. During brain development, Hevin is expressed in the radial glia and controls a detachment process that terminates neuronal migration in the pial surface of the cerebral cortex[18]. Hevin is also secreted from neural stem cells (NSCs) in the lateral ventricle subventricular zone (SVZ) and enhances glioma cell invasion[19]. Thus, it appears likely that Hevin is involved in cell migration and invasion in a context-dependent manner. Importantly, it has been reported that Hevin reinforces the synaptic connectivity in the cerebral cortex[20]. On this occasion, Hevin interacts with both Neurexin 1α (NRX1α) and Neuroligin 1B (NL1B) and promotes a trans-synaptic bridge at thalamocortical synaptic connections in the cerebral cortex. Hevin has also been reported to enhance the NMDAR-mediated synapse response[21]. Strikingly, genome-wide association studies have revealed that multiple mutations in the *SPARCL1* gene increase the risk of ASD[5], indicating that Hevin plays an important role in regulating synaptic connectivity and the brain environment.

A recent structural analysis reported that Hevin promotes the interaction between NRXs and NLs[22]. Hevin is composed of a flexible acidic region at the N-terminal region, a follistatin-like (FS) domain at the center region, and an extracellular calcium (EC) binding domain, including two EF-hand motifs (EF-hand 1: His^{586}-Ala^{618} and EF-hand 2: His^{625}-Phe^{651} amino acid in humans, EF-hand 1: His^{572}-Ala^{604} amino acid and EF-hand 2: His^{611}-Phe^{637} amino acid in mice) at the C-terminal region. Interestingly, the structure of the FS/EC region of Hevin differs from that of Sparc, although Sparc shares high sequence identity with Hevin. The FS-domain is crucial for promoting the bridge between NRXs and NLs. Hevin and Sparc compete to interact with NLs via the FS-domain, and thereby Sparc can thus antagonize the synaptogenic functions of Hevin. In contrast, the EC-domain in both Hevin and Sparc interacts with the extracellular matrix, such as Collagen I and V, in a Ca^{2+}-dependent manner[22,23]. Therefore, analyzing the functions of the EC domain is key to understanding the full functions of Hevin.

In this study, we analyzed the importance of the EF-hand motif in Hevin. We found that the integrity of the EF-hand motif is necessary for proper trafficking to the extracellular space. In addition, a single amino acid substitution in the EF-hand motif, which is associated with ASD, causes Hevin to accumulate in the ER and activates the UPR pathway. These findings suggest the possibility that protein accumulation due to improperly folded Hevin contributes to ASD pathogenesis.

Results

Hevin mutants lacking the EF-hand motif are generated in the *Usp15*-deficient brain. Previously, we have reported that USP15 influences the spliceosome cascade and UPR pathway despite the unclear relevance[11] (Fig. 1A). Thus, we looked for ASD-associated abnormal variants that changed splicing upon *Usp15* deficiency and are involved in the UPR pathway. In this context, we checked the expression profile dataset obtained from mice brains[11] and found that the 3'-region of the hevin transcript tends to be lacking in the *Usp15*-deficient brains (Fig. 1B, Supplementary Table S1). Thus, we speculated that the 3'-region of the hevin transcript is susceptible to abnormalities in the spliceosome cascade regulated by USP15. We determined which base sequence of the hevin transcript was altered in the *Usp15*-deficient brain. To do this, we conducted a 3'-rapid amplification of cDNA ends (3'-RACE) and identified two 3'-fragments lacking the EF-hand motif. One was the EF-hand deletion mutant and the other was the trans-splicing variant, which fused with a fragment of NADH: ubiquinone oxidoreductase subunit A11 (Ndufa11) (Fig. 1C–G). Because the EF-hand motif is pivotal for regulating protein structure and functions[24], we hypothesized that EF-hand deletion mutants show abnormal structure, resulting in a decrease of secretion efficiency.

Hevin mutants lacking the EF-hand motif activate the UPR signaling caused by abnormal trafficking. To investigate whether these mutants are secreted to the extracellular space, we constructed the expression plasmids of full-length Hevin mutants and transfected them into culture cells. Although Hevin WT was efficiently secreted to the extracellular space, the deletion mutant of EF-hand 2 (Hevin ΔEF) and the fusion protein between Hevin lacking the EF-hand and Ndufa11 C-terminal region (Hevin-N11) showed reduced secretion efficiency compared to Hevin WT (Fig. 2A). These data suggest that the integrity of the EF-hand motifs is crucial for the secretion of Hevin. We next examined whether Hevin mutants accumulate in the ER. To do this, we introduced each plasmid into HeLa cells and stained using an anti-Hevin antibody. Consequently, Hevin mutants were found to be prone to accumulate in the ER compared to Hevin WT (Fig. 2B,C). These data demonstrate that an abnormal EF-hand region suppresses a Hevin export from the ER. Next, we examined whether the accumulation of Hevin mutants activates the UPR pathway. The expression of both Hevin ΔEF and Hevin-N11 increased the mRNA of the UPR markers, *Bip* and *Chop* (Fig. 2D,E). Moreover, the protein level of

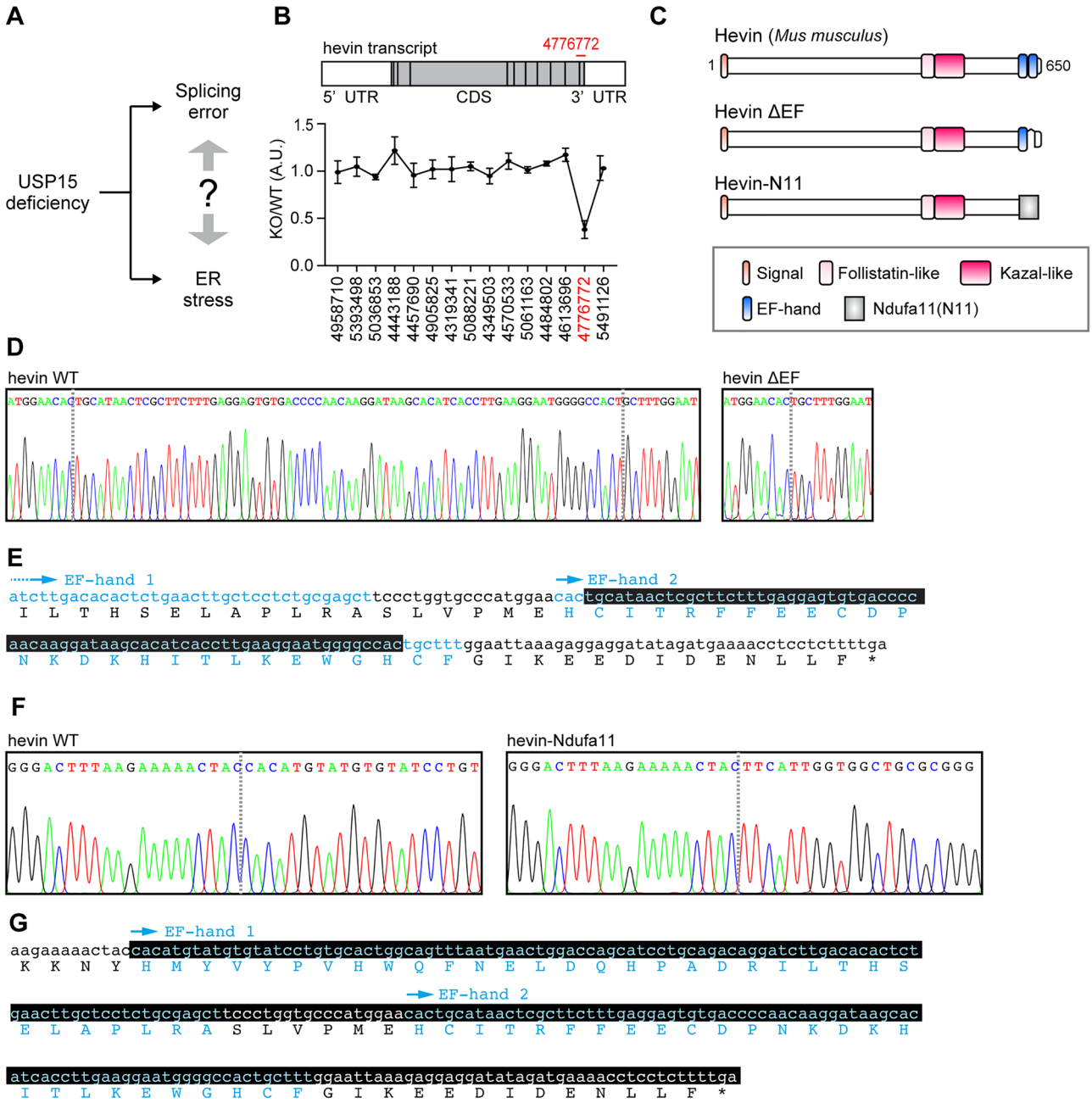

Figure 1. Hevin mutants lacking the EF-hand motif are generated in the *Usp15*-deficient brain. (**A**) The relationship between the splicing error and ER stress in the *Usp15*-deficient brain has not yet clarified. (**B**) Schematic structure of the hevin transcript in the *Usp15*-deficient mouse brain. The 3'-region of the hevin transcript (PSR/Junction ID: 4,776,772) is prone to be missing in the *Usp15*-deficient brain. (**C**) The putative schematic structures of Hevin mutants. (**D**–**G**) Sequence analyses of the 3'-regions of hevin transcripts. (**D**) DNA sequencing chromatogram of the 3'-region of hevin WT and ΔEF transcripts. (**E**) The 3'-region of hevin sequence. Black box indicates the lacking sequence in ΔEF mutant. Cyan indicates the EF-hand motif. (**F**) DNA sequencing chromatogram of the 3'-region of hevin WT and Ndufa11. (**G**) The 3'-region of hevin sequence. Black box indicates the lacking sequence in the Hevin-N11 mutant. Cyan indicates the EF-hand motif.

BIP, which is the ER chaperone protein, was increased when Hevin mutants were expressed. Importantly, the BIP expression level was similar to that of thapsigargin-stimulated cells (Fig. 2F), suggesting that Hevin EF-hand deletion mutants accumulate in the ER and activate the UPR pathway.

ASD-associated W647R mutation of Hevin activates the UPR signaling. Both *SPARCL1* and *Usp15* mutations are associated with ASD[2,5,9,10]. Importantly, previous transcriptome analyses have identified single amino acid substitutions in SPARCL1/Hevin that are linked to ASD[5]. One of these mutants in which

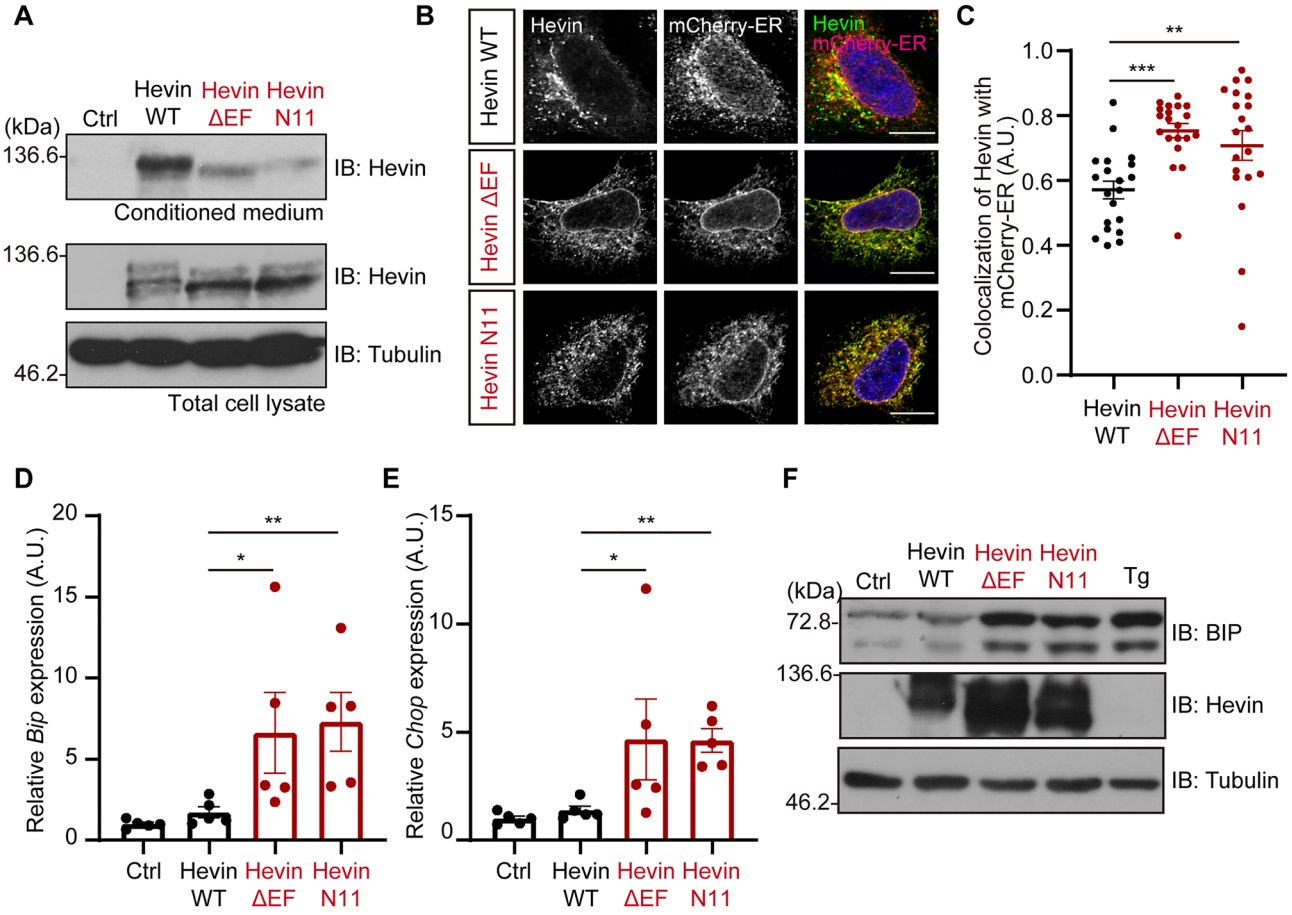

Figure 2. Hevin mutants lacking the EF-hand motif activate the UPR signaling caused by abnormal trafficking. (**A**) Immunoblotting of Hevin WT and mutants (ΔEF and N11). Neuro-2a cells were transfected for 48 h with expression vectors for Hevin WT or mutants (ΔEF or N11). The cell lysates and conditioned medium were subjected to immunoblot analysis using anti-Hevin and Tubulin antibodies. (**B**) Immunostaining of Hevin and mutants (ΔEF and N11). HeLa cells were transfected for 24 h with expression vectors for Hevin and mCherry-ER and subjected to immunocytochemistry. Scale bar: 10 μm. (**C**) Quantification of Pearson's correlation coefficient as the degree of colocalization in the panel B. n = 20 cells, mean ± standard error of the mean (SEM), $^{**}p < 0.01$, $^{***}p < 0.001$ versus Hevin WT, one-way analysis of variance (ANOVA) Dunnett's test. (**D**, **E**) Total RNAs isolated from the Hevin-overexpressed Neuro-2a cells were conducted with qPCR analysis for measurement of Bip and Chop mRNAs. 5S rRNAs were used for normalization. n = 5; mean ± SEM; $^{*}p < 0.05$, $^{**}p < 0.01$ versus Hevin WT, one-way ANOVA Dunnett's test calculated using the ΔCt value. (**F**) Immunoblotting of BIP, Hevin, and Tubulin. HEK293T cells were transfected for 72 h with expression vectors for Hevin WT or mutants (ΔEF or N11). Cells were stimulated with 500 nM Thapsigarging (Tg) for 24 h. The cells were then subjected to immunoblot analysis using anti-BIP, Hevin and Tubulin antibodies.

Trp^{647} is replaced with Arg is in the EF-hand motif that is also perturbed in *Usp15* knockouts[5] (Fig. 3A, Supplementary Fig. 1). Strikingly, this amino acid is highly conserved among aves, rodents, and primates (Fig. 3B). Therefore, we postulated that this mutant [human W647R (hW647R)] could exhibit a similar cellular phenotype to the truncated Hevin mutants that we observed in *Usp15* KO mice in Fig. 2. First, to investigate whether this amino acid substitution in the EF-hand motif affects Hevin trafficking, we constructed an expression plasmid using the mouse Hevin sequence. Since human Trp^{647} corresponds to mouse Trp^{633} (Fig. 3B), we replaced mouse Trp^{633} with Arg [mouse W633R (mW633R)]. As we expected, the secretion efficiency in Hevin mW633R was attenuated compared to that in Hevin WT (Fig. 3C). In addition, the Hevin mW633R mutant was mostly localized in the ER, as well as Hevin ΔEF and Hevin-N11 (Fig. 3D and E) and was not transported to the Golgi apparatus efficiently (Fig. 3F and G). Furthermore, the expression of Hevin mW633R increased the mRNA level of the UPR markers, *Bip* and *Chop*, and the protein level of BIP (Fig. 3H–J), suggesting that a single amino acid substitution in the EF-hand causes Hevin accumulation in the ER, followed by activation of the UPR signaling. Next, we investigated the mechanisms through with the Hevin mutant increases ER stress. Since unfolded proteins promote dissociation of BIP from the ER stress sensors such as IRE1, leading to interaction with freed BIP, we examined whether Hevin mW633R exhibits unfolded protein-like behavior. We found that the binding affinity of Hevin mW633R to BIP is higher than that of WT (Fig. 3K and L). Importantly, Ca^{2+} existence has little

effect on this binding. These data suggest that the Hevin mW633R mutant induces improper folding regardless of Ca^{2+} existence and supports our idea that the Hevin mutant exhibits a different structure compared to WT.

Hevin W647R mutant shows improper folding of the hydrophobic core. Because BIP tends to recognize the hydrophobic sites of misfolded proteins[25,26], we speculate that the Hevin WR mutant exhibits structural instability. To verify this hypothesis, a set of μs-order all-atom molecular dynamics (MD) simulations was performed for the EC domain (515–664 amino acid) of WT and hW647R mutant (Fig. 4A). As the first analysis of both trajectories, the root-mean-square deviation (RMSD) for each initial structure during each MD simulation was calculated. As shown in the RMSD profiles, the hW647R system structurally fluctuated compared to the WT system since the hW647R RMSD value increased during the MD simulations, indicating that a replacement of Trp^{647} with Arg causes an structural instability (Supplementary Fig. 2A–D). To address the origin of this structural fluctuation, the solvent-accessible surface area (SASA) was measured in both systems. It is reasonable to measure the SASA values to address the mutational effect since the structural fluctuation might be caused by a protein surface deformation, in which a part of the protein surface of the WT system might be exposed to the external solvent upon this amino acid substitution. For all of the residues included within 8 Å around the mutation site, their SASA distributions significantly changed in shape, and the SASA values increased in the hW647R system compared to the WT system (Fig. 4B and C). These analyses indicate that this amino acid substitution causes structural fluctuation of the hW647R system. As the second analysis, the radial distribution function (RDF) of water was defined for all of the residues included within 8 Å around the mutation site. The RDFs around each residue allow for identifications of the essential residues that increase SASA. Among all of the calculated distributions, the RDFs of water around V520 showed characteristic profiles (Fig. 4D), where the RDF around V520 for the hW647R system significantly increased compared to that for the WT system. This increase in RDF indicates that the water density around V520 became higher due to the point mutation. Based on the difference in these RDFs, the difference in the density of water was compared among the corresponding residues as follows:

$$\sum_r \Delta g(r) = \sum_r g(r)_{WT} - g(r)_{W647R}.$$

From the decomposed accumulation, we focused on the top ten residues with the especially large RDF differences (Fig. 4E). Based on the structural observation in the WT system, the hydrophobic residues included in the top ten residues had showed characteristic properties, that is, they tightly contacted each other and constructed a core site. Notably, this core formed in the WT system was not formed in the hW647R system (Fig. 4F and G). To evaluate the structural changes of the hydrophobic core quantitively, the radius of gyration (R_g) of seven hydrophobic residues was measured. The R_g value of these hydrophobic residues characterizes the size of each hydrophobic core. The distributions of R_g differed between the two systems (Fig. 4H,I). Specifically, the median value of R_g measured in the WT system was 8.847 Å while that measured in the hW647R system was 9.675 Å, indicating that the hydrophobic core of the hW647R system was changed. Therefore, it is likely that Hevin hW647R has improper folding around the hydrophobic residues, resulting in structural instability.

Discussions

In this study, we identified that the defects in the Hevin EF-hand motif decrease secretion efficiency and accumulate in the ER. In addition, the ASD-associated Hevin mutant also shows impaired trafficking and hampered an export from the ER. Indeed, the Hevin mutant exposes a hydrophobic region, which is normally hidden inside, to the surface, inhibiting the export of Hevin from the ER and activating the UPR pathway (Fig. 5). Thus, our findings provide a potential mechanism that links an ASD mutation in the *SPARCL1* gene to UPR.

Here, we found that this single amino acid substitution in the EF-hand has two cellular phenotypes. First, the expression of Hevin WR activates the UPR pathway. Second, the mutation attenuates the secretion efficiency. As such, we presume that the activation of the UPR pathway and/or the decrease of secretion efficiency are possible mechanisms that connect the Hevin dysfunctions to ASD. Previously, ER stress was proposed as a cellular mechanism related to the onset of ASD[27]. In fact, the UPR-related transcripts are dysregulated in the frontal cortices of ASD patients[28]. In most cases of regulating the UPR, three distinct pathways, the inositol-requiring enzyme 1 (IRE1)—X-box binding protein 1 (XBP1) pathway, protein kinase R-like ER kinase (PERK)—eukaryotic initiation factor 2α (eIF2α) pathway, and activating transcription factor 6 (ATF6) pathway, are upregulated by the ER stress, such as abnormal Ca^{2+} homeostasis in the ER and perturbed ER-Golgi trafficking. Because Hevin is predominantly expressed in astrocytes, it is likely that the perturbed the UPR pathways in astrocytes could be an important mechanism underlying ASD pathogenesis. A key question for future research is the biological relevance of how the ER stress response in astrocytes contributes to neural circuits and brain homeostasis. In *Caenorhabditis elegans*, overexpression of Xbp1 in astrocyte-like glial cells extends the life span via changing neuropeptide secretion machinery[29]. This observation demonstrates that upregulation of the UPR in astrocyte-like glial cells is pivotal for regulating ER stress resistance and longevity, exhibiting a positive effect in nematodes. Interestingly, a mutation in *Xbp1* is responsible for the onset of bipolar disorder[30]. Hence, these results raise the interesting hypothesis that dysfunctions of the Xbp1 axis could also regulate both neurodevelopmental and psychiatric disorders. In contrast, overactivation of PERK-eIF2α signaling in astrocytes causes neuronal loss and neurodegeneration in mice[31]. Strikingly, impaired UPR signaling markedly changes their secretory factors from astrocytes, suggesting that each UPR signaling in astrocytes regulates the surrounding cells in a non-cell-autonomous manner. Thus, it is plausible that the upregulation of ER stress induced by Hevin WR may change the global secretome, resulting in circuit dysfunction that is causal to ASD. Another possibility is that UPR signaling controls the timing of neural and glial differentiation. For instance, OASIS, a subfamily of ATF6,

Figure 3. ASD-associated W647R mutant of Hevin activates the UPR signaling. (**A**) Location of ASD-associated Hevin mutations. (**B**) Amino acid of the EF-hand motif in each species. The human Trp^{647} is highly conserved. Cyan indicates the EF-hand motif, Magenta indicates non-conserved amino acid. (**C**) Immunoblotting of Hevin WT and mW633R mutant. Neuro-2a cells were transfected with expression vectors and collected at the indicated times. The upper panel indicates the experimental schedule. The transfection efficiencies were confirmed by observing co-expressed EGFP fluorescence. The cell lysates and conditioned medium were subjected to immunoblot analysis using anti-Hevin and Tubulin antibodies. The secretion rate of the Hevin WR mutant was delayed more than that of WT. CM; conditioned medium, TCL: total cell lysate (**D**) Immunostaining of Hevin WT and mW633R mutant. HeLa cells were transfected for 24 h with expression vectors for Hevin and mCherry-ER and subjected to immunocytochemistry. Scale bar: 10 µm. (**E**) Quantification of Pearson's correlation coefficient as the degree of colocalization in the panel D. n = 15 cells, mean ± SEM, $***p < 0.001$ by Student's *t*-test. (**F**) Immunostaining of Hevin and mW633R mutant. HeLa cells were transfected for 24 h with expression vectors for Hevin and subjected to immunocytochemistry. Scale bar: 10 µm. (**G**) Quantification of Manders' coefficient as the degree of colocalization of Hevin with GM130 in the panel F. n = 20 cells, mean ± SEM, $***p < 0.001$ by Student's *t*-test. (**H**, **I**) Total RNAs isolated from the Hevin-overexpressed Neuro-2a cells were conducted with qPCR analysis for measurement of *Bip* and *Chop* mRNAs. 5S rRNA were used for normalization. n = 5; $**p < 0.01$, $***p < 0.001$ versus Hevin WT, one-way ANOVA Dunnett's test calculated *p*-value using the ΔCt value. (**J**) Immunoblotting of BIP, Hevin, and Tubulin. Neuro-2a cells were transfected for 72 h with expression vectors for Hevin WT or mW633R mutants. The cell lysates were then subjected to immunoblot analysis using anti-BIP, Hevin, and Tubulin antibodies. (**K**) Schematic structure of GST-Hevin. (**L**) Pull down of GST-Hevin and endogenous BIP in HEK293T cells. GST-Hevin was precipitated with Glutathione Sepharose beads and immunoblotted with anti-GST, BIP, and Tubulin antibodies.

controls proper UPR signaling and regulates astrocyte differentiation in the embryonic stage[32]. Since perturbed glial differentiation brings about developmental disorders, it is plausible that Hevin mutant-induced ER stress during the embryonic period influences glial differentiation, leading to the development of ASD. Previously, various maternal immune activations (MIAs), such as exposures to environmental irritants and infections with pathogens, have been reported to cause ASD. Intriguingly, MIA activates the PERKs-eIF2α pathway and inhibits new protein synthesis. Either genetic or pharmacological inhibition of this pathway improves MIA-induced ASD-like behavior[33], supporting the idea that ER stress is related to ASD.

Hevin promotes synaptogenesis through stabilizing the interaction between NRX1α and NL1B[20]. The structure of Hevin is divided into three main parts, the acidic domain, FS domain, and EC domain[22]. The FS domain binds to NRX1α and NL1B concurrently, and the EC domain, of Hevin, including the EF-hand motif, is predicted to be essential for interacting with the collagen in a Ca^{2+}-dependent manner[22,23]. We found that only a small amount of the Hevin mW633R mutant can be secreted to the extracellular space even in a mutation of the EF-hand. These data imply that exposure to the hydrophobic region of the C-terminus may result in the acquiring of novel functions that disturb innate functions in the extracellular space even in the presence of Ca^{2+}. One hypothesis is that the binding affinity between Hevin and collagen proteins is changed and affects the functions of synaptogenesis. Ehlers-Danlos syndromes, which exhibit autism-like phenotypes, arise from mutation in *Col1A* and *Col5A* genes[34]. Therefore, the Hevin WR mutant could also impact the conditions of the extracellular matrix and brain microenvironment. Previous studies have reported that Sparc, a homolog of Hevin, suppresses synaptogenesis. Intriguingly, the deletion mutant lacking an acidic domain (SLF) exhibits a similar phenotype as Sparc in which SLF suppresses synaptogenesis[35]. Hevin is also cleaved at the center region (approximately 350 amino acids) by a metalloprotease, ADAMTS4, and produces the fragment containing both FS and EC domains[36]. Therefore, it is likely that Hevin hW647R mutant acquires a distinct function, like Sparc and SLF. However, further studies will be needed to clarify this possibility in the future.

Previous studies have reported that other mutations in the *SPARCL1 gene* associated with ASD have been revealed, and most mutations reside in the FS domain and EC domain[5] (see Fig. 3A). Mutations in which Thr^{516} and Met^{587} are replaced with Met and Ile, respectively, are next to the residue (Asp^{517} and Tyr^{588}) with large RDF differences. Thus, it is likely that the native hydrophobic core is unfolded when these amino acids are substituted. ASD-associated amino acid substitutions around the EF-hand motif may change the native hydrophobic core, resulting in a fluctuated structure of Hevin. Notably, Ca^{2+} deprivation has less effect on the binding between BIP and the Hevin WR mutant. Thus, it is plausible that exposure of the hydrophobic region covered not only by Trp^{647} but also by Thr^{516} and Met^{587} impairs Hevin secretion and synaptogenesis, regardless of Ca^{2+}.

In summary, here we found that the EF-hand motif in Hevin plays an important role for proper trafficking to the extracellular spaces. A loss of this domain causes protein accumulation in the ER and activates the UPR pathway. Furthermore, we found that ASD-associated mutation in which Trp^{647} is replaced with Arg exhibits a similar phenotype in cells. Importantly, in the hW647R mutant Hevin the hydrophobic core of the EF hand is exposed to the surface likely causing structural instability. Taken together, our findings provide multiple molecular mechanisms linking an ASD point mutation in the *SPARCL1* gene with cellular phenotypes underlying the onset of ASD.

Materials and methods

Plasmids. Mouse Hevin cDNA was amplified from pMD-mSPARCL1 (Sino Biological Inc. MG50544-M) and cloned into pCRblunt. The deletion mutant of EF-hand (Hevin ΔEF) was constructed using the inverse plymerase chain reaction (PCR) method. Briefly, Hevin ΔEF cDNA was amplified from pCRblunt-Hevin, followed by conducting a T4 polynucleotide kinase reaction (TAKARA). After phosphorylation, this fragment was self-ligated and constructed a circular plasmid as a pCRb-Hevin ΔEF. The Hevin-Ndufa11 (Hevin-N11) frag-

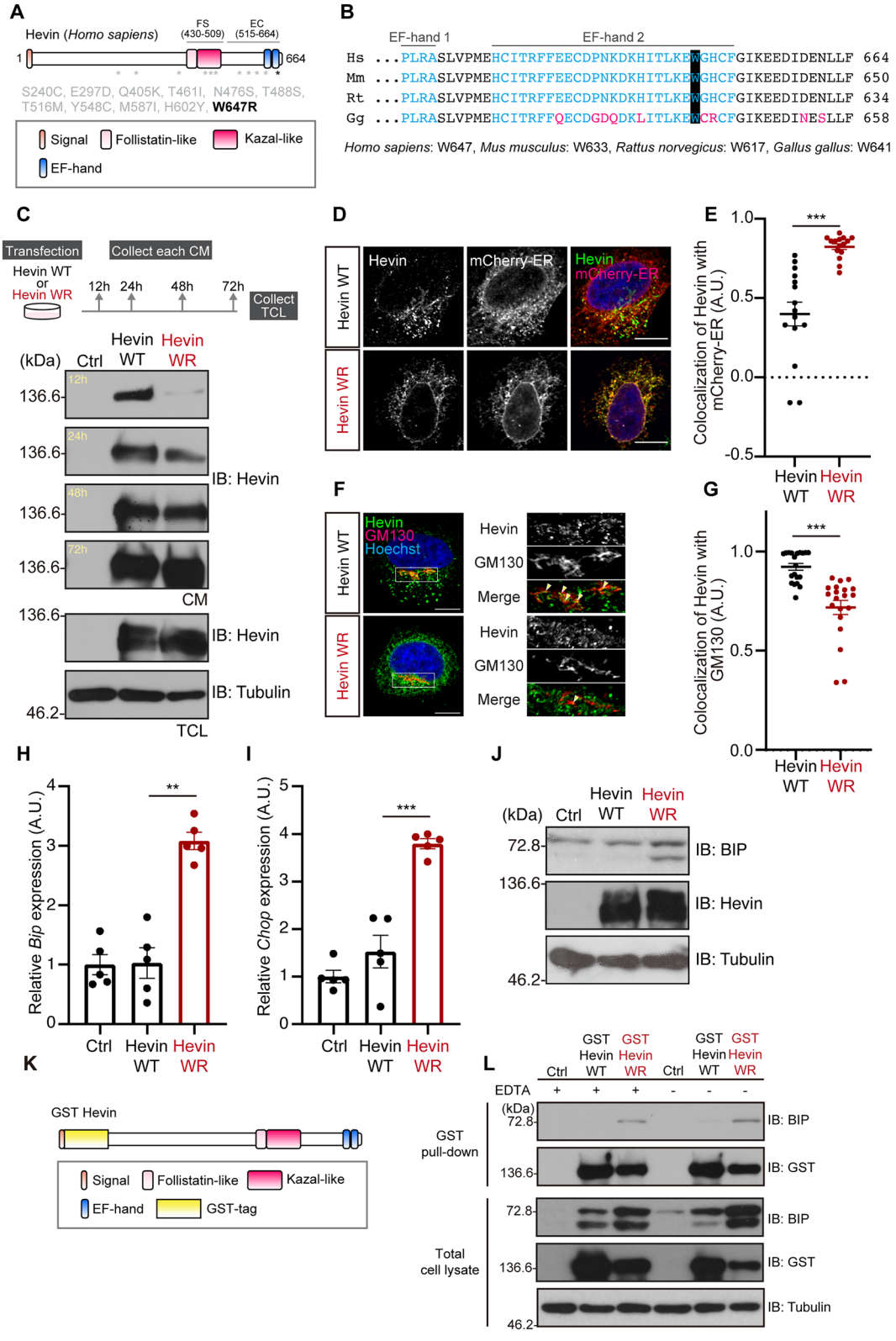
A
Hevin (Homo sapiens)
FS (430-509)
EC (515-664)
1
664
S240C, E297D, Q405K, T461I, N476S, T488S, T516M, Y548C, M587I, H602Y, W647R
Signal
Follistatin-like
Kazal-like
EF-hand
B
EF-hand 1
EF-hand 2
Hs ...PLRASLVPMEHCITRFFEECDPNKDKHITLKEWGHCFGIKEEDIDENLLF 664
Mm ...PLRASLVPMEHCITRFFEECDPNKDKHITLKEWGHCFGIKEEDIDENLLF 650
Rt ...PLRASLVPMEHCITRFFEECDPNKDKHITLKEWGHCFGIKEEDIDENLLF 634
Gg ...PLRASLVPMEHCITRFFQECDGDQDKLITLKEWCRCFGIKEEDINESLLF 658
Homo sapiens: W647, Mus musculus: W633, Rattus norvegicus: W617, Gallus gallus: W641
C
Transfection
Collect each CM
Hevin WT or Hevin WR
12h 24h 48h 72h
Collect TCL
(kDa) Ctrl Hevin WT Hevin WR
136.6
IB: Hevin
CM
IB: Hevin
IB: Tubulin
46.2
TCL
D
Hevin WT
Hevin WR
Hevin
mCherry-ER
Hevin mCherry-ER
E
Colocalization of Hevin with mCherry-ER (A.U.)
1.0
0.5
0.0
-0.5
***
Hevin WT
Hevin WR
F
Hevin WT
Hevin WR
Hevin
GM130
Hoechst
Merge
G
Colocalization of Hevin with GM130 (A.U.)
1.0
0.5
0.0
***
Hevin WT
Hevin WR
H
Relative Bip expression (A.U.)
4
3
2
1
0
**
Ctrl
Hevin WT
Hevin WR
I
Relative Chop expression (A.U.)
5
4
3
2
1
0
***
Ctrl
Hevin WT
Hevin WR
J
(kDa) Ctrl Hevin WT Hevin WR
72.8
IB: BIP
136.6
IB: Hevin
46.2
IB: Tubulin
K
GST Hevin
Signal
Follistatin-like
Kazal-like
EF-hand
GST-tag
L
Ctrl
GST Hevin WT
GST Hevin WR
Ctrl
GST Hevin WT
GST Hevin WR
EDTA + + + - - -
(kDa)
GST pull-down
72.8
IB: BIP
136.6
IB: GST
Total cell lysate
72.8
IB: BIP
136.6
IB: GST
46.2
IB: Tubulin

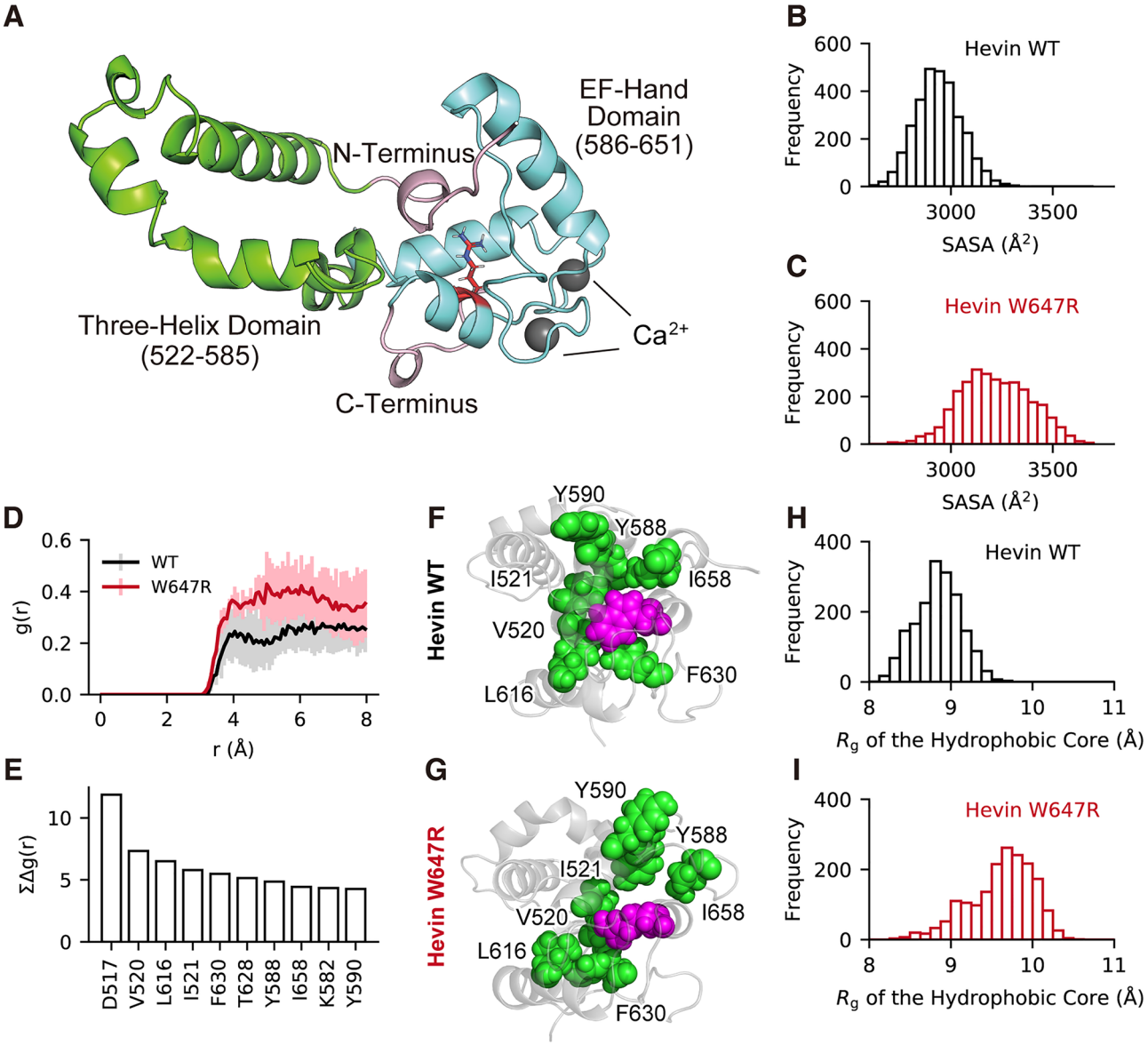

Figure 4. Hevin W647R mutant shows improper folding of the hydrophobic core. (**A**) The modeled structure of the WT Hevin system (EC domain). Each color represents the three-helix domain (green), EF-hand domain (cyan), and the N or C terminals (pink), respectively. The spheres (grey) represent Ca^{2+} ions. The structure is reconstituted from the data in the previous research[22] (**B**, **C**) The SASA distribution of all of the residues included within 8 Å around the mutation site. (**D**) Characteristic RDFs of water around V520 with their standard deviations. (**E**) The accumulation of the difference in the RDFs of water between the WT and W647R systems, i.e., $\sum_r \Delta g(r) = \sum_r g(r)_{WT} - g(r)_{W647R}$, versus the top ten residues. (**F**, **G**) A set of configurations of each hydrophobic core (D517, V520, L616, I521, F630, T628, Y588, I658, K582 and Y590), where the hydrophobic core and mutated residues are highlighted in green and magenta. (**H**, **I**) The Rg distributions of each hydrophobic core.

ment was amplified from Hevin cDNA and Ndufa11 cDNA was obtained from the 3'-RACE method; next, these fragments were ligated using an In-Fusion system (TAKARA). The Hevin-N11 fragment was inserted into the pCR-blunt using the In-Fusion system. The gene encoding Hevin mW633R was generated by a quick-change method using KOD polymerase. The GST-Hevin proteins were generated by the SLiCE method[37]. Briefly, the full-length Hevin cDNA was amplified using KOD plus DNA polymerase (TOYOBO) and inserted into the BglII sites of pCS4 vector. The GST-tagged Hevin and Hevin mW633R mutant were generated using the SLiCE reaction. The GST fragment was subcloned from pGEX-6P-1 plasmid into the site between the Hevin signal-peptide and another part using the SLiCE reaction. The primers used were as follows:

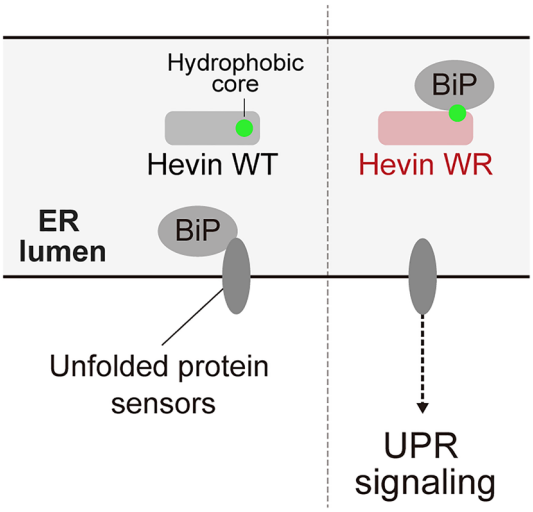

Figure 5. Model describing the dynamics of Hevin WT and WR mutant in the ER. BIP associates with Hevin WR mutant and triggers the UPR activation.

Full-length Hevin forward, 5′-aaagatctgccaccatgaaggctgtgcttctcc-3′;
Full-length Hevin reverse, 5′-ggagatcttcaaaagaggaggttttcatctatatcctcctc-3′;
Hevin ΔEF inverse sense, 5′-tgctttggaattaaagaggaggatatagatg -3′;
Hevin ΔEF inverse antisense, 5′-gtgttccatgggcaccaggg-3′;
N-terminal Hevin forward, 5′-gctggaattcaggagtgaaggctgtgcttc-3′;
N-terminal Hevin reverse, 5′-gatggtctccagccaagagtctcttctcatcc-3′;
C-terminal Hevin-Ndufa11 mutants forward, 5′-gagactcttggctggagaccatcccattg-3′;
C-terminal Hevin-Ndufa11 mutants reverse, 5′-tctgcagaattcaggacaccttgggggtag-3′;
Hevin W633R mutant forward, 5′-gaaggaacggggccactgc-3′;
Hevin W633R mutant reverse, 5′-gcagtggccccgttccttc-3′;
Hevin (pCS4) for SLiCE forward, 5′-tcgtgacatcccgacaagtacaaggtttctctc-3′;
Hevin (pCS4) for SLiCE reverse, 5′-tataggggatgccacagcggttcccaag-3′;
GST for SLiCE forward, 5′-ctgtggcatcccctatactaggttattgg-3′;
GST for SLiCE reverse, 5′-ttgtcgggatgtcacgatgcgg-3′;

3′-rapid amplification of cDNA ends (3′-RACE). Total RNAs from WT and *USP15*-deficient brains were isolated by ISOGEN II (NIPPON GENE) according to the manufacturer's instructions. The cDNAs were synthesized by reverse transcriptase and 100 units of ReverTra Ace (TOYOBO) together with 25 pmol random hexamer primer (TOYOBO), 20 nmol dNTPs, and total RNAs. The 3′-region of the hevin transcript was determined using the 3′-RACE method. First-strand synthesis was conducted using the Hevin outside primer and Hevin adaptor primer. Then, the second round of PCR was conducted using the Hevin inside primer and Hevin amplification primer. The 3′-fragment amplified by 3′-RACE was inserted into the pCR-blunt and the DNA sequences were analyzed. The primers used were as follows:

Hevin outside primer, 5′-aaatgctgaaccttcagatgagggc-3′;
Hevin adaptor primer, 5′-ggccacgcgtcgactagtacttttttttttttttt-3′;
Hevin inside primer, 5′-agagactcttggctggagaccatc-3′;
Hevin amplification primer, 5′-ggccacgcgtcgactagtac-3′;

Antibodies. For immunoblotting goat anti-Hevin (1:1000, R&D Systems, Cat# AF2836), mouse anti-Tubulin (1:1000, Sigma, DM1A), rabbit anti-BIP (1:1000, Cell Signaling, CB0B12), and mouse anti-GST (1:500, Santa Cruz, B14) antibodies were used as primary antibodies. Horseradish peroxidase-conjugated anti-mouse IgG, anti-rabbit IgG, and anti-goat IgG (1:20,000, respectively, SeraCare) antibodies were used as secondary antibodies. For immunofluorescence, rabbit anti-RFP (1:500, Rockland, Cat# 600-401-379), goat anti-Hevin (1:500, R&D Systems, Cat# AF2836), and mouse anti-GM130 (1:500, MBL, Cat# M179-3) were used as primary antibodies. Alexa Fluor 488 donkey anti-goat IgG H&L (1:500, Thermo Fisher Scientific), DyLight 594 donkey anti-rabbit IgG H&L (1:500, abcam), and DyLight 594 donkey anti-mouse IgG H&L (1:500, abcam) antibodies were used as secondary antibodies.

Cell culture and transfection. HEK293T[38,39] cells and HeLa cells[38,39] were cultured in Dulbecco's modified Eagle's medium (high glucose) (Wako) containing 5% fetal bovine serum (FBS), 100 units penicillin, and 100 mg streptomycin (P/S Thermo Fisher Scientific). Cells were transfected using polyethyleneimine MAX (PEI Max) (Polyscience). The amounts of the plasmids and PEI Max were optimized in proportion to the relative

surface area and number of cells. Cells were plated at 1.5 to 5.0×10^5 cells in 4 ml per 60 mm dish and incubated at 5% CO_2 and 37 °C for 1 day. The plasmids (8.0—16.0 μg) were mixed with 500 μl of Opti-MEM (Thermo Fisher); 1.0 μg/μl of PEI Max (32.0—64.0 μl) was mixed with 500 μl of Opti-MEM in another tube. Both solutions were combined and incubated for 20 min at room temperature, followed by adding these mixtures to cells. After incubation for 1 h, the media were changed to fresh culture medium. Neuro-2a cells were cultured in Eagle's minimum essential medium (Wako) containing 10% FBS and P/S. Cells were plated at 1.5×10^5 cells on a 6-well plate and incubated at 5% CO_2 and 37 °C for 1 day. The plasmids (4.0 μg) were mixed with 250 μl of Opti-MEM (Thermo Fisher); and 1.0 μg/μl of PEI Max (8.0 μl) was mixed with 250 μl of Opti-MEM in another tube. Both solutions were combined and incubated for 20 min at room temperature, followed by adding these mixtures to cells. After incubation for 4 h, the media were changed to fresh culture medium. HeLa cells and 293 T cells were obtained from American Type Culture Collection (ATCC, US). Neuro-2A cells were obtained from JCRB Cell Bank (NIBIOHN, Japan).

Immunocytochemistry. HeLa cells were plated at 5.0×10^4 cells and incubated on 15 mm coverslips on a 12-well plate for 1 day and then transfected with indicated plasmids. After the incubation for 24 h, the cells were washed in PBS and fixed with 4% paraformaldehyde (Merck KGaA) in PBS for 10 min at 4 °C. The coverslips were washed in PBS and blocked with 5% bovine serum albumin (BSA; Wako) in PBS with 0.4% Triton X-100 (MP Biomedicals), then incubated with primary antibodies diluted in blocking solution overnight at 4 °C. After washing with PBS, the cells were incubated with secondary antibodies diluted in blocking solution for 30 min at room temperature. Nuclei were stained with 10 μg/ml Hoechst 33,342 (Life Technologies). The coverslips were then mounted onto slides using FLUOROSHIELD Mounting Medium (ImmunoBioScience). Fluorescent images were obtained using confocal laser scanning fluorescence microscopy (ZEISS, LSM700) with a 63x (Plan-Apochromat 63x/1.4 Oil DIC) or 100x (αPlan-Apochromat 100x/1.46 Oil DIC) objective. The diode excitation lasers (Diode 405, Diode 488, and Diode 555) were operated and directed to a photomultiplier tube (LSM T-PMT, Carl Zeiss) through a series of band pass filters (Ch1:BP420-475 + BP500-610, Ch2:BP490-635, and Ch3:BP585-1000).

Colocalization analysis. Colocalization analysis of immunofluorescence signals was performed according to the previous study[40]. The colocalization values (Pearson's co-efficients or Manders' co-efficients) were calculated using the immunofluorescence signals of Hevin and either mCherry-ER or GM130 from representative images by Fiji plugin Coloc-2. All data were reproduced in at least two independent experiments.

GST pull-down assay. HEK293T cells were plated at 5.0×10^5 cells and incubated for 1 day and then transfected with indicated plasmids. After the incubation for 48 h, cells were washed with PBS and collected with lysis buffer [20 mM Tris–HCl (pH 7.5), 150 mM NaCl, 0.5% NP-40, 1 mM DTT, 1 mM PMSF, 3 μg/ml leupeptin, 3 μg/ml Pepstatin A, and 5 μg/ml aprotinin] in the presence or absence of 1 mM EDTA. Cell lysates were centrifuged at 14,000 rpm for 5 min. The supernatants were mixed with Glutathione Sepharose beads (GE Healthcare) and then incubated for 2 h at 4 °C with rotation. The precipitants were washed 3 times with lysis buffer and subjected to immunoblot analysis. All data were reproduced in at least two independent experiments.

Immunoblot analysis. HEK293T cells or Neuro-2a cells were plated at 0.8 or 1.5×10^5 cells on a 6-well plate and incubated at 37 °C with 5% CO_2 for 1 d. Cells were transfected and then incubated for 3 days. The cells were collected with lysis buffer [20 mM Tris–HCl (pH 7.5), 150 mM NaCl, 1 mM EDTA, 0.5% NP-40, and 1 mM DTT]. Cell lysates were centrifuged at 14,000 rpm for 5 min. The supernatant was run on SDS-PAGE for protein separation, followed by electrophoretic transfer to a polyvinylidene difluoride membrane (Pall). After 1 h blocking by 5% skim milk at room temperature, membranes were incubated with primary antibodies overnight at 4 °C. The proteins on the membranes were then detected with HRP-conjugated secondary antibodies and chemiluminescence reagents (Chemi-Lumi One Super, Nacalai Tesque). All data were reproduced in at least two independent experiments.

Quantitative real-time PCR (qPCR). Neuro-2a cells (1.5×10^5 cells/ 6-well plate) were cultured for 24 h and then transfected with indicated plasmids. After the incubation for 48 h, the cells were washed in PBS and collected with ISOGEN II (NIPPON GENE). Total RNAs from cells were isolated according to the ISOGEN II manufacturer's instructions. The cDNAs were synthesized by reverse transcriptase, 100 units ReverTra Ace (TOYOBO) together with 25 pmol Random Primer (nonamer; TOYOBO), 20 nmol dNTPs and 500 ng total RNAs. Quantitative (q)PCR was performed on a 96-well plate (Scientific Specialties) using THUNDERBIRD SYBR qPCR Mix (TOYOBO) in an Applied Biosystems 7900HT Fast Real Time PCR System (Applied Biosystems). The relative quantity of the target expression was calculated by $2^{-\Delta\Delta Ct}$ methods using SDS Software 2.4.2 (Applied Biosystems) with the following calculation. The relative quantity = $2^{-\Delta\Delta Ct}$, $\Delta\Delta Ct = (Ct^{target} - Ct^{5S})_{sample} - (Ct^{target} - Ct^{5S})_{reference}$; Ct, threshold cycle. All data were reproduced in at least two independent experiments. The primers used were as follows:

5S rRNA forward, 5′-cggccataccaccctgaac-3′;
5S rRNA reverse, 5′-gcggtctcccatccaagtac-3′;
BiP forward, 5′-gagactgctgaggcgtattt-3′;
BiP reverse, 5′-cctcatgacattcagtccag-3′;
Chop forward, 5′-ctggaagcctggtatgaggat-3′;
Chop reverse, 5′-cagggtcaagagtagtgaaggt-3′;

Molecular dynamics (MD) simulation. The WT and W647R systems of Hevin were prepared to conduct an MD simulation. In each system, only the EC domain (511–663) of Hevin was considered. The WT and mutant (W647R) systems were modeled using a crystal structure (PDB code: 7KBU)[22]. To model the W647R system, this amino acid substitution was induced using the Pymol program (The PyMOL Molecular Graphics System, Version 2.0 Schrödinger, LLC.). In each system, the missing amino acid residues were added using the SWISS-MODEL program[41]. The modeled structures were solvated with the TIP3P water model[42] in an orthorhombic box. The LINCS[43] and SETTLE[44] algorithms were adopted to extend the MD time step to 2 fs. The modified Berendsen thermostat[45] and Parrinello–Rahman method[46,47] controlled the temperatures and pressures of all systems, respectively. The particle mesh Ewald method[48] evaluated electrostatic interactions using a real-space cutoff value of 10 Å. The cutoff value for the van der Waals interactions was set to 10 Å. All of the MD simulations were performed with the GPU version of the GROMACS 2020 package[49] using the Amber 14SBonlysc force field[50]. Before conformational sampling, energy minimizations on the initially modeled systems removed the steric crashes of atoms. Subsequently, 100-ps *NVT* ($T = 300$ K) and 100-ps *NPT* ($T = 300$ K and $P = 1$ bar) MD simulations relaxed each system. Lastly, the final snapshots of the *NPT* simulations on each system were specified as the starting configurations of their production runs. To generate statistically reliable MD trajectories, multiple 1-μs MD simulations (1-μs × 3 runs for each system) were independently started from each relaxed configuration by regenerating their initial velocities. Finally, the first 0.4-μs trajectories were considered as the equilibration phase, and the remaining 0.6-μs trajectories were used for analyses in each system.

Statistical analysis. Prism ver.8.4.3 software (GraphPad Software, Inc.) was used for all statistical analyses. Statistical significance was analyzed using Student's *t*-test and analysis of variance (ANOVA) followed by Dunnett's test.

Data availability

The GEO accession number for the array data set is GSE145385[11]. The PDB code of the Hevin crystal structure is 7KBU[22]. The authors declare no competing interests.

Received: 13 April 2022; Accepted: 29 June 2022
Published online: 13 July 2022

References

1. Sanders, S. J. *et al.* De novo mutations revealed by whole-exome sequencing are strongly associated with autism. *Nature* **485**, 237–241. https://doi.org/10.1038/nature10945 (2012).
2. O'Roak, B. J. *et al.* Sporadic autism exomes reveal a highly interconnected protein network of de novo mutations. *Nature* **485**, 246–250. https://doi.org/10.1038/nature10989 (2012).
3. O'Roak, B. J. *et al.* Multiplex targeted sequencing identifies recurrently mutated genes in autism spectrum disorders. *Science* **338**, 1619–1622. https://doi.org/10.1126/science.1227764 (2012).
4. Iossifov, I. *et al.* The contribution of de novo coding mutations to autism spectrum disorder. *Nature* **515**, 216–221. https://doi.org/10.1038/nature13908 (2014).
5. De Rubeis, S. *et al.* Synaptic, transcriptional and chromatin genes disrupted in autism. *Nature* **515**, 209–215. https://doi.org/10.1038/nature13772 (2014).
6. Das, T., Song, E. J. & Kim, E. E. The multifaceted roles of USP15 in signal transduction. *Int. J. Mol. Sci.* https://doi.org/10.3390/ijms22094728 (2021).
7. Menzies, F. M. *et al.* Autophagy induction reduces mutant ataxin-3 levels and toxicity in a mouse model of spinocerebellar ataxia type 3. *Brain* **133**, 93–104. https://doi.org/10.1093/brain/awp292 (2010).
8. Cornelissen, T. *et al.* The deubiquitinase USP15 antagonizes Parkin-mediated mitochondrial ubiquitination and mitophagy. *Hum. Mol. Genet.* **23**, 5227–5242. https://doi.org/10.1093/hmg/ddu244 (2014).
9. Chen, R. *et al.* Leveraging blood serotonin as an endophenotype to identify de novo and rare variants involved in autism. *Mol. Autism* **8**, 14. https://doi.org/10.1186/s13229-017-0130-3 (2017).
10. Krupp, D. R. *et al.* Exonic Mosaic mutations contribute risk for autism spectrum disorder. *Am. J. Hum. Genet.* **101**, 369–390. https://doi.org/10.1016/j.ajhg.2017.07.016 (2017).
11. Kim, J. *et al.* USP15 deubiquitinates TUT1 associated with RNA metabolism and maintains cerebellar homeostasis. *Mol. Cell Biol.* https://doi.org/10.1128/MCB.00098-20 (2020).
12. Zhang, C. *et al.* A neuroligin-4 missense mutation associated with autism impairs neuroligin-4 folding and endoplasmic reticulum export. *J. Neurosci.* **29**, 10843–10854. https://doi.org/10.1523/JNEUROSCI.1248-09.2009 (2009).
13. Wang, J. *et al.* Endoplasmic reticulum retention and degradation of a mutation in SLC6A1 associated with epilepsy and autism. *Mol. Brain* **13**, 76. https://doi.org/10.1186/s13041-020-00612-6 (2020).
14. Fujita, E. *et al.* Autism spectrum disorder is related to endoplasmic reticulum stress induced by mutations in the synaptic cell adhesion molecule, CADM1. *Cell Death Dis.* **1**, e47. https://doi.org/10.1038/cddis.2010.23 (2010).
15. Falivelli, G. *et al.* Inherited genetic variants in autism-related CNTNAP2 show perturbed trafficking and ATF6 activation. *Hum. Mol. Genet.* **21**, 4761–4773. https://doi.org/10.1093/hmg/dds320 (2012).
16. Chen, S. *et al.* Regulation of SPARC family proteins in disorders of the central nervous system. *Brain Res. Bull.* **163**, 178–189. https://doi.org/10.1016/j.brainresbull.2020.05.005 (2020).
17. Risher, W. C. *et al.* Astrocytes refine cortical connectivity at dendritic spines. *Elife* https://doi.org/10.7554/eLife.04047 (2014).
18. Gongidi, V. *et al.* SPARC-like 1 regulates the terminal phase of radial glia-guided migration in the cerebral cortex. *Neuron* **41**, 57–69. https://doi.org/10.1016/s0896-6273(03)00818-3 (2004).
19. Qin, E. Y. *et al.* Neural precursor-derived pleiotrophin mediates subventricular zone invasion by Glioma. *Cell* **170**, 845-859 e819. https://doi.org/10.1016/j.cell.2017.07.016 (2017).
20. Singh, S. K. *et al.* Astrocytes assemble thalamocortical synapses by bridging NRX1alpha and NL1 via hevin. *Cell* **164**, 183–196. https://doi.org/10.1016/j.cell.2015.11.034 (2016).
21. Gan, K. J. & Sudhof, T. C. Specific factors in blood from young but not old mice directly promote synapse formation and NMDA-receptor recruitment. *Proc. Natl. Acad. Sci. U S A* **116**, 12524–12533. https://doi.org/10.1073/pnas.1902672116 (2019).
22. Fan, S., Gangwar, S. P., Machius, M. & Rudenko, G. Interplay between hevin, SPARC, and MDGAs: Modulators of neurexin-neuroligin transsynaptic bridges. *Structure* **29**, 664-678 e666. https://doi.org/10.1016/j.str.2021.01.003 (2021).

23. Hambrock, H. O. *et al.* SC1/hevin. An extracellular calcium-modulated protein that binds collagen I. *J. Biol. Chem.* **278**, 11351–11358. https://doi.org/10.1074/jbc.M212291200 (2003).
24. Grabarek, Z. Structural basis for diversity of the EF-hand calcium-binding proteins. *J. Mol. Biol.* **359**, 509–525. https://doi.org/10.1016/j.jmb.2006.03.066 (2006).
25. Flynn, G. C., Pohl, J., Flocco, M. T. & Rothman, J. E. Peptide-binding specificity of the molecular chaperone BiP. *Nature* **353**, 726–730. https://doi.org/10.1038/353726a0 (1991).
26. Gething, M. J. & Sambrook, J. Protein folding in the cell. *Nature* **355**, 33–45. https://doi.org/10.1038/355033a0 (1992).
27. Kawada, K. & Mimori, S. Implication of endoplasmic reticulum stress in autism spectrum disorder. *Neurochem. Res.* **43**, 147–152. https://doi.org/10.1007/s11064-017-2370-1 (2018).
28. Crider, A., Ahmed, A. O. & Pillai, A. Altered expression of endoplasmic reticulum stress-related genes in the middle frontal cortex of subjects with autism spectrum disorder. *Mol. Neuropsychiatry* **3**, 85–91. https://doi.org/10.1159/000477212 (2017).
29. Frakes, A. E. *et al.* Four glial cells regulate ER stress resistance and longevity via neuropeptide signaling in *C. elegans*. *Science* **367**, 436–440. https://doi.org/10.1126/science.aaz6896 (2020).
30. Kakiuchi, C. *et al.* Impaired feedback regulation of XBP1 as a genetic risk factor for bipolar disorder. *Nat. Genet.* **35**, 171–175. https://doi.org/10.1038/ng1235 (2003).
31. Smith, H. L. *et al.* Astrocyte unfolded protein response induces a specific reactivity state that causes non-cell-autonomous neuronal degeneration. *Neuron* **105**, 855-866 e855. https://doi.org/10.1016/j.neuron.2019.12.014 (2020).
32. Saito, A. *et al.* Unfolded protein response, activated by OASIS family transcription factors, promotes astrocyte differentiation. *Nat. Commun.* **3**, 967. https://doi.org/10.1038/ncomms1971 (2012).
33. Kalish, B. T. *et al.* Maternal immune activation in mice disrupts proteostasis in the fetal brain. *Nat. Neurosci.* **24**, 204–213. https://doi.org/10.1038/s41593-020-00762-9 (2021).
34. Casanova, E. L., Baeza-Velasco, C., Buchanan, C. B. & Casanova, M. F. The relationship between Autism and Ehlers-Danlos syndromes/hypermobility spectrum disorders. *J. Pers. Med.* https://doi.org/10.3390/jpm10040260 (2020).
35. Kucukdereli, H. *et al.* Control of excitatory CNS synaptogenesis by astrocyte-secreted proteins Hevin and SPARC. *Proc. Natl. Acad. Sci. U S A* **108**, E440-449. https://doi.org/10.1073/pnas.1104977108 (2011).
36. Weaver, M. S. *et al.* Processing of the matricellular protein hevin in mouse brain is dependent on ADAMTS4. *J. Biol. Chem.* **285**, 5868–5877. https://doi.org/10.1074/jbc.M109.070318 (2010).
37. Motohashi, K. A simple and efficient seamless DNA cloning method using SLiCE from Escherichia coli laboratory strains and its application to SLiP site-directed mutagenesis. *BMC Biotechnol.* **15**, 47. https://doi.org/10.1186/s12896-015-0162-8 (2015).
38. Tsuruta, F. *et al.* SCFFbl12 Increases p21Waf1/Cip1 Expression Level through Atypical Ubiquitin Chain Synthesis. *Mol. Cell. Biol.* **36**, 2182–2194. https://doi.org/10.1128/MCB.00174-16 (2016).
39. Ebina, M. *et al.* Myeloma overexpressed 2 (Myeov2) regulates L11 subnuclear localization through Nedd8 modification. *PLoS One* **8**, e65285. https://doi.org/10.1371/journal.pone.0065285 (2013).
40. Dunn, K. W., Kamocka, M. M. & McDonald, J. H. A practical guide to evaluating colocalization in biological microscopy. *Am. J. Physiol. Cell Physiol.* **300**, C723-742. https://doi.org/10.1152/ajpcell.00462.2010 (2011).
41. Waterhouse, A. *et al.* SWISS-MODEL: Homology modelling of protein structures and complexes. *Nucleic Acids Res.* **46**, W296–W303. https://doi.org/10.1093/nar/gky427 (2018).
42. Jorgensen, W. L., Chandrasekhar, J., Madura, J. D., Impey, R. W. & Klein, M. L. Comparison of simple potential functions for simulating liquid water. *J. Chem. Phys.* **79**, 926–935. https://doi.org/10.1063/1.445869 (1983).
43. Hess, B., Bekker, H., Berendsen, H. J. C. & Fraaije, J. G. E. M. LINCS: A linear constraint solver for molecular simulations. *J. Comput. Chem.* **18**, 1463–1472. https://doi.org/10.1002/(Sici)1096-987x(199709)18:12%3c1463::Aid-Jcc4%3e3.0.Co;2-H (1997).
44. Miyamoto, S. & Kollman, P. A. Settle-an analytical version of the shake and rattle algorithm for rigid water models. *J. Comput. Chem.* **13**, 952–962. https://doi.org/10.1002/jcc.540130805 (1992).
45. Bussi, G., Donadio, D. & Parrinello, M. Canonical sampling through velocity rescaling. *J. Chem. Phys.* **126**, 014101 (2007).
46. Parrinello, M. & Rahman, A. Crystal-structure and pair potentials-a molecular-dynamics study. *Phys. Rev. Lett.* **45**, 1196–1199. https://doi.org/10.1103/PhysRevLett.45.1196 (1980).
47. Parrinello, M. & Rahman, A. Polymorphic transitions in single-crystals-a new molecular-dynamics method. *J. Appl. Phys.* **52**, 7182–7190. https://doi.org/10.1063/1.328693 (1981).
48. Essmann, U. *et al.* A smooth particle mesh ewald method. *J. Chem. Phys.* **103**, 8577–8593. https://doi.org/10.1063/1.470117 (1995).
49. Abraham, M. J., van der Spoel, D., Lindahl, E., Hess, B. & team, t. G. d. GROMACS User Manual version 2019. (2019).
50. Maier, J. A. *et al.* ff14SB: Improving the accuracy of protein side chain and backbone parameters from ff99SB. *J. Chem. Theory Comput.* **11**, 3696–3713. https://doi.org/10.1021/acs.jctc.5b00255 (2015).

Acknowledgements

We thank the lab members for helpful discussions and technical support. MD simulations were partially performed with a supercomputer (Cygnus) provided by the Multidisciplinary Cooperative Research Program (MCRP) in the Center for Computational Sciences (CCS), University of Tsukuba, Japan (Project Code: LSC and MOLBIO). This work was supported by Grants-in Aid from the Ministry of Education, Science, Sports and Culture of Japan JSPS KAKENHI (16K07339, 16KK0158, 20K05951), the Astellas Foundation for Research on Metabolic Disorders, and the Gout and Uric Acid Foundation of Japan to FT. CE is an HHMI Investigator.

Author contributions

T.T. and F.T. designed the research; T.T., T.Y., R.M., J.K. and F.T. performed experiments; T.T., T.Y., R.M., J.K., R.H., and F.T. analyzed the data; and T.T., T.Y., R.H., C.E., and F.T. wrote the paper. Study supervision: Y.S., C.E., and F.T.

Competing interests

The authors declare no competing interests.

Additional information

Supplementary Information The online version contains supplementary material available at https://doi.org/10.1038/s41598-022-15784-5.

Correspondence and requests for materials should be addressed to F.T.

Reprints and permissions information is available at www.nature.com/reprints.